Available online at www.sciencedirect.com

ScienceDirect

Acta Materialia 92 (2015) 64–71

Acta MATERIALIA

www.elsevier.com/locate/actamat

Effect of porosity on the magneto-mechanical behavior of polycrystalline magnetic shape-memory Ni–Mn–Ga foams

C. Witherspoon,[a,1] P. Zheng,[b] M. Chmielus,[a,c,2] D.C. Dunand[b] and P. Müllner[a,*]

[a]*Department of Materials Science and Engineering, Boise State University, Boise, ID 83725, USA*
[b]*Department of Materials Science & Engineering, Northwestern University, Evanston, IL 60208, USA*
[c]*M-I1, Helmholtz Centre Berlin for Materials and Energy, Hahn-Meitner-Platz 1, 14109 Berlin, Germany*

Received 15 June 2013; revised 17 January 2015; accepted 10 March 2015
Available online 13 April 2015

Abstract—Porosity in polycrystalline Ni–Mn–Ga alloys reduces internal constraints imposed by grain boundaries which suppress magnetic-field-induced strain in non-porous, polycrystalline magnetic shape-memory alloys. We present here a systematic study of the porosity effect on the magneto-mechanical properties of polycrystalline Ni–Mn–Ga foams. Starting from replicated foams created by casting with ceramic space holders, their porosities were increased by successive acid dissolution steps after which the magnetic-field-induced strain was measured, for each porosity level, after thermo-magneto-mechanical training. Consistently, the magnetic-field-induced strain increased with increasing porosity, in the extreme case by one order of magnitude for a small porosity increase of 1.3%, demonstrating that removal of constraints by porosity is responsible for the high magnetic-field-induced strain in polycrystalline Ni–Mn–Ga foams.

Keywords: Martensitic phase transformation; Foam architecture; Thermal cycling; Ni_2MnGa; Heusler alloys

1. Introduction

Magnetic shape-memory alloys (MSMAs) have gained much attention due to their large and repeatable reversible magnetic-field-induced strains (MFIS) resulting from twin boundary motion induced by a variation of a magnetic field [1–4]. In particular, off-stoichiometric Ni_2MnGa (referred to as Ni–Mn–Ga in the following) alloys are very promising candidates for applications in actuators and sensors, as they exhibit MFIS of 6%–10% as single crystals [5,6]. To date, most researchers have thus focused on single crystals, but the difficulty of preventing composition drift due to elemental evaporation and the solidification segregation associated with single-crystal production hinder the production of affordable materials with reproducible properties. Polycrystalline materials show chemical homogeneity and have much lower production costs, but they are not widely studied due to a near-zero MFIS [7,8]. The cause for this absence of MFIS is the suppression of twin boundary motion by grain boundaries, or equivalently the strain incompatibility between misoriented neighboring grains. To reduce the hindrance on twin boundary motion in polycrystals (or grain incompatibility), a high degree of texture may be introduced, e.g. via directional solidification and annealing, thus improving the MFIS values achievable to 0.3% [9–14].

Another approach to increase MFIS in polycrystalline Ni–Mn–Ga is to introduce pores in the structure which reduce internal constraints between neighboring grains [15–17]. Ni–Mn–Ga with a monomodal pore size distribution demonstrated MFIS of 0.12%, much larger than 0.025% reported values for non-porous, small-grained Ni–Mn–Ga alloys [15]. Grain incompatibilities were further reduced in foams with a bimodal pore size distribution, where large struts and nodes between large pores contained a population of smaller pores. These foams with hierarchical porosity sizes achieved very large MFIS of up to 8.7% [16,17]. It can be expected that increasing pore fraction, while maintaining a given pore architecture, should result in an increase in MFIS by reducing constraints. This hypothesis is tested in the present article, and results are discussed in terms of percolation of a network of hard and soft links [18–21].

2. Experimental procedures

As described previously [15,16], open-porous foams were created by replication casting using a preform of sodium aluminate ($NaAlO_2$) space-holder powders with bimodal

* Corresponding author.
[1] Present address: Micron Technology, Boise, ID 83716, USA.
[2] Present address: Department of Mechanical Engineering & Materials Science, University of Pittsburgh, Pittsburgh, PA 15261, USA.

http://dx.doi.org/10.1016/j.actamat.2015.03.038
1359-6462/

size. The partially sintered preforms, with a nominal porosity of ~50%, consisted of a 73:27 (by weight) blend of large (size: 500–600 μm) and small (size: 75–90 μm) $NaAlO_2$ powders. The blended powders were poured into an alumina crucible with an internal diameter of 9.53 mm and lightly sintered in air at 1500 °C for 3 h to create necks between powders, ensuring no displacement of powders occurred during melt infiltration. A $Ni_{52}Mn_{24.3}Ga_{23.7}$ ingot – created by induction melting in Ar of a mixture of 99.9% pure Ni pellets (from ESPI), electrolytic Mn flakes (from Alfa Aesar), and 99.999% pure Ga pellets (from Alfa Aesar) – was placed on top of the sintered preform. The assembly was heated to 1200 °C at 7 °C/min under a vacuum of 3.5×10^{-6} Torr (4.7×10^{-4} Pa). This temperature was maintained for 24 min before high-purity argon gas was introduced in the furnace at a pressure of 1.34 atm to push the molten alloy into the preform. At the same time, the temperature was dropped at a rate of 7 °C/min to 1000 °C. The alloy was homogenized at that temperature for 1 h and then subjected to a stepwise heat-treatment to establish the $L2_1$ structure (725 °C/2 h, 700 °C/10 h, 500 °C/20 h) before being cooled to ambient temperature.

Three parallelepiped specimens (labeled A, B, C) were cut with dimensions of $\sim 6 \times 3 \times 2\ mm^3$ with a diamond saw from two cast Ni–Mn–Ga/$NaAlO_2$ composites, A and B belonging to the first and C to the second. Most of the $NaAlO_2$ powders were removed by immersion in 34% H_2SO_4 under sonication at 24 ± 5 °C for ~10 h. The specimens were then immersed in 10% HCl at 25 ± 9 °C under sonication to remove the remaining $NaAlO_2$ space-holder and to increase porosity by metal dissolution, a method used previously for open-porous aluminum and Ni–Mo–Cr foams [22,23].

The Ni–Mn–Ga foams were characterized with respect to their phase transformation, composition, architecture/microstructure, and porosity. The structural and magnetic phase transformations were characterized with a vibrating sample magnetometer (VSM, EDA Technologies, Model 10) by heating and cooling the foam in a low magnetic field of 25 mT at a heating or cooling rate of 8.5 °C/min. Magnetic anisotropy was also tested with the VSM by increasing field and measuring magnetization relative to different directions of the sample. To quantify only magneto-crystalline anisotropy, shape anisotropy was corrected by subtracting the internal field NH_{ext}, where N is the demagnetization factor and H_{ext} is the applied magnetic field. The area between the two M–H curves with the field parallel to the easy and hard axis of magnetization was integrated to give the magneto-crystalline anisotropy energy. Chemical compositions were determined with a Hitachi S3400 N-II scanning electron microscope (SEM) equipped with an integrated Oxford EDS system. The compositions of all foams were measured at the same instrument setting (i.e. at constant accelerating voltage, probe current and working distance) calibrated with a Ni–Mn–Ga standard specimen whose chemical composition had been measured independently by wet chemical analysis. A Leo 1430 VP SEM was used to characterize the foam architecture and microstructure. Porosity was determined by measurement of mass and volume.

MFIS was determined by exposing the foams to a rotating magnetic field of 0.97 T. Thermo-magneto-mechanical cycling (TMC) was carried out during field rotation while heating and cooling the foam through the phase transformation. TMC allows for *in situ* observation of the phase transformation, thermo-magneto-mechanical training, and measurement of MFIS produced by a foam in a fully martensitic state. Heating and cooling of the foam was achieved through introduction of hot and cold air into the specimen chamber. The foam temperature was measured via a thermocouple in direct contact to the foam. The temperature was averaged over one revolution of the magnetic field, and the maximum MFIS for one magnet revolution was plotted against the temperature. The detection limit of MFIS in the TMC experiment was 0.01% for experiments with variable temperature and 0.002% for experiments at constant ambient temperature. The larger experimental error in experiments with variable temperature originated from the forced air flow. A detailed description of the TMC experiment is given in Ref. [16].

3. Results

The phase transformation temperatures of the three foams are listed in Table 1 and mutually agreed within 3 °C except for the martensite finish temperature, M_f, of Foam B, which were 8 and 10 °C higher than that of Foams A and C, respectively. All foams were cooled below M_f (below room temperature) to ensure that they were fully martensitic during TMC.

Table 2 lists the compositions of the three foams after removal of the space-holder. Deviations from the nominal parent ingot composition were within experimental error. The chemical composition of Foam A was monitored with EDS after every dissolution step and remained unchanged, confirming that dissolution was not selective for a particular element, but removed the alloy uniformly.

The magnetic anisotropy, after correction for shape-anisotropy, of Foams A and C were 39.1 and 37.1 kJ/m^3, which is about 20% of the magneto crystalline anisotropy energy of a single crystal [24]. The magnetic anisotropy energy of Foam B was 10.5 kJ/m^3, which is only about 5% of the magneto crystalline anisotropy energy of a single crystal. It is inferred from these low values that Foam B was very close to randomly textured whereas Foams A and C had a weak texture.

Fig. 1a and b show MFIS vs. temperature plots for Foam C subjected to TMC cycles at the initial porosity level (Fig. 1a, porosity of 71%) and after metal dissolution (Fig. 1b and c, porosity of 72.3%). In Fig. 1a, the maximum MFIS in the martensite was 0.12% and it decreased to 0.01% when heated to 50 °C, as expected from the foam transforming to austenite. However, no sharp austenite–martensite (A–M) phase transformation was reflected in the form of a rapid MFIS change over a few °C, implying that the transformation occurred over a wide temperature range. By increasing the porosity of this foam by acid dissolution by only 1.3% (from 71.0% to 72.3%), the MFIS increased fivefold to ~0.6%, as measured for the first

Table 1. Martensite start and finish temperatures (M_s and M_f), austenite start and finish temperatures (A_s and A_f), and Curie temperature (T_c).

Foam	M_s [°C]	M_f [°C]	A_s [°C]	A_f [°C]	T_C [°C]
A	27	14	22	37	99
B	24	22	20	33	90
C	26	12	22	35	95

Table 2. Compositions of Foams A, B and C compared to their nominal parent ingot composition.

Foam	Ni (at.%)	Mn (at.%)	Ga (at.%)
Nominal composition	52.0	24.3	23.7
A	51.7 ± 2.6	24.5 ± 1.3	23.7 ± 2.8
B	51.6 ± 1.8	24.9 ± 0.8	23.4 ± 1.8
C	50.7 ± 1.8	24.8 ± 1.1	24.4 ± 0.6

two TMC (Fig. 1b). A further doubling to 1.25% occurred for the following two TMC (Fig. 1c). The martensitic phase transformation hysteresis appeared clearly in the form of a sharp drop of MFIS: from 27 to 36 °C upon heating for the martensite–austenite (M–A) phase transformation, and from 22 to 11 °C upon cooling for the A–M phase transformation. For the first TMC (Fig. 1b, black squares) the MFIS was 0.58% at −10 °C and decreased upon heating to 0.27% at 27 °C when the M–A phase transformation started. The MFIS was below the detection limit in the austenite phase. Upon subsequent cooling, the A–M phase transformation started at 22 °C, after which the MFIS followed the same path of strain increase up to 0.58% at −10 °C at the end of the first cycle. The subsequent TMC 2–4 showed a very flat region of MFIS while heating (from −10 to 30 °C). However, on cooling, the MFIS increased past the intersection of the heating curve up to a maximum MFIS at ∼10 °C followed by a decrease in MFIS. For example TMC 2 showed a MFIS of 0.45% from −5 to 30 °C until the M–A phase transformation starts. Upon cooling through the A–M transformation, the MFIS increased to 0.84% at 10 °C followed by a decrease to 0.55% at −10 °C. For TMCs 2–4, in the martensitic state, the MFIS vs. temperature paths were not the same on heating and cooling, in contrast to TMC 1. Repeated TMC resulted in an increase of MFIS from one TMC to the next. The maximum MFIS was 0.62% for TMC 1 and reached 1.25% for TMC 4. After a second dissolution step, the foam could no longer be tested because it developed a large cavity making handling impossible. SEM images were taken after the last magneto-mechanical test (Fig. 1c). The micrograph (Fig. 1d) shows severe cracking accompanied by the mutual displacement of opposite crack surfaces, which had formed during TMC.

Foam B displayed an increase in MFIS over multiple dissolution steps. Fig. 2 shows a TMC for foam B at three different porosities. With increasing porosity, the martensite transformation displayed more clearly in the MFIS values. Upon heating through the reverse transformation, the MFIS dropped to near zero around 30 °C. Upon cooling, the MFIS rose quickly between 15 and 10 °C. The maximum MFIS increased with each porosity increase.

Fig. 3 shows the maximum MFIS value for each TMC as a function of porosity for the three foams. Each foam showed an increasing trend of MFIS with increasing porosity, as shown by the lines in Fig. 3 representing linear fit determined for each foam individually. Foam A showed a maximum MFIS of 0.26% during thermal cycling at a porosity of 48.5% which increased to 0.27% when the porosity was increased to 52.3%. The MFIS further

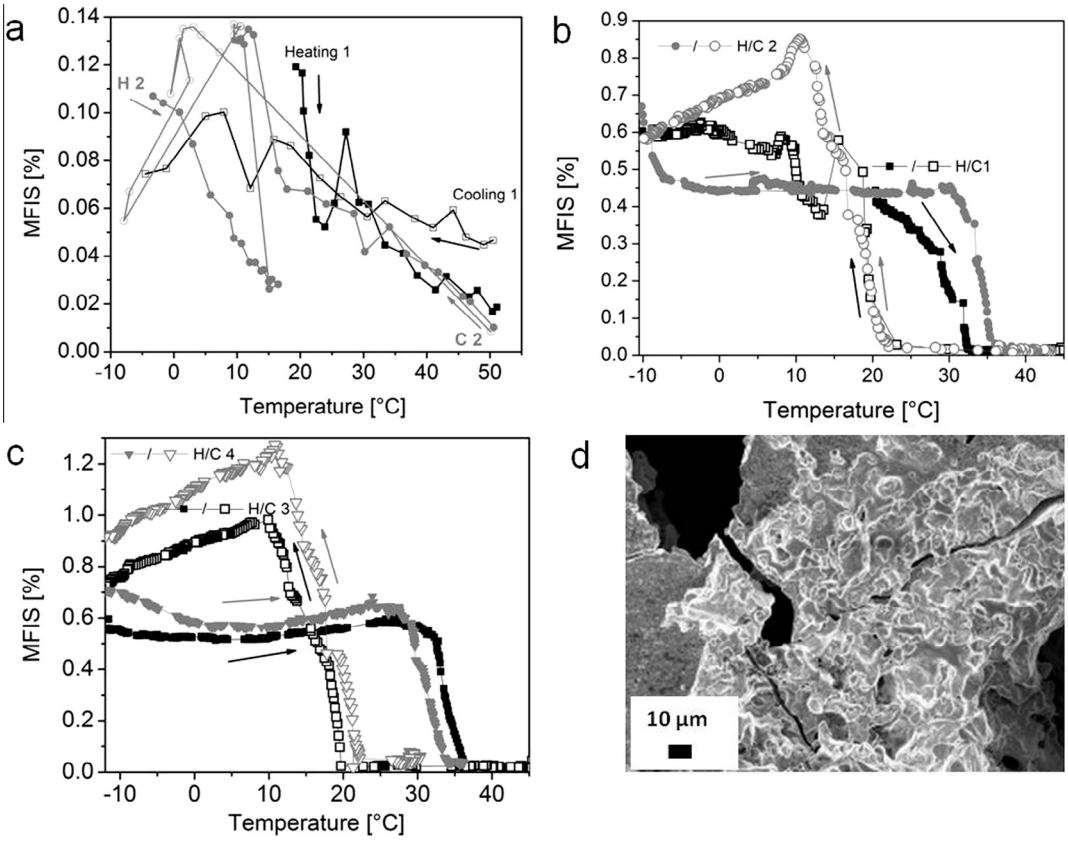

Fig. 1. Plot of MFIS vs. temperature for Foam C at (a) 71.0% porosity (original value); (b) 72.3% porosity during TMCs 1 and 2; (c) 72.3% porosity during TMCs 3 and 4. Heating is shown with full symbols and cooling with hollow symbols; TMCs are numbered. (d) SEM picture of Foam C showing cracked struts.

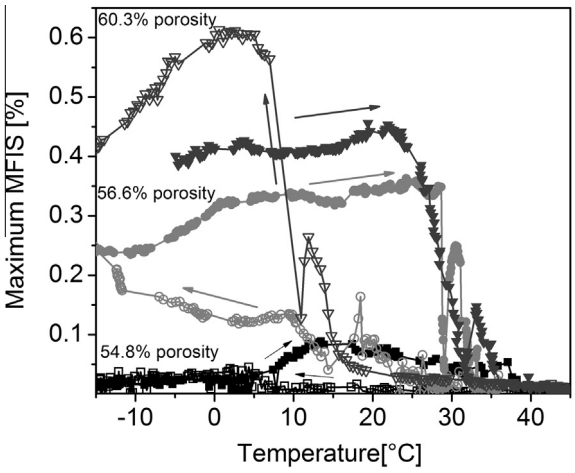

Fig. 2. Plot of MFIS vs. temperature for Foam B at three different porosities. Only the TMC with the highest MFIS is shown: TMC 2 for porosities of 54.8 and 56.6%, TMC 3 for 60.3% porosity. Heating is shown with full symbols and cooling with hollow symbols.

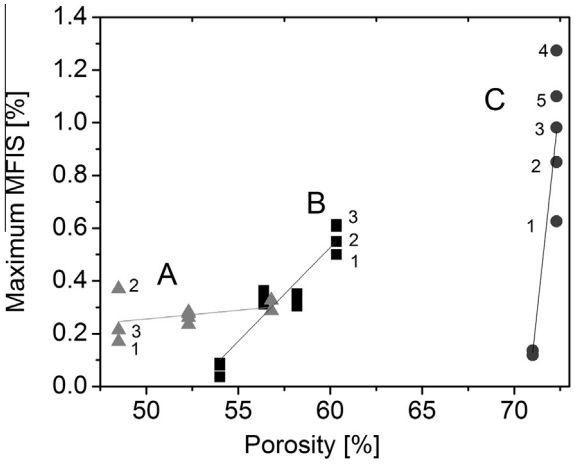

Fig. 3. Porosity dependence of maximum MFIS for each TMC (numbered) for Foams A, B, and C.

increased to 0.29% when the porosity was increased to 56.8%. Foam B initially showed a maximum MFIS of 0.09% during thermal cycling, at a porosity of 54%, increasing steadily with porosity to a value of 0.61% for 60.3% porosity. Finally, Foam C showed a tenfold increase in maximum MFIS observed during thermal cycling from 0.12% to 1.26% with an increase in porosity from 71% to 72.3%.

4. Discussion

4.1. Binary model of percolating strut networks

For each of the three foams, the MFIS increased as porosity was increased by alloy dissolution, without changing any other variable such as crystallographic texture, composition, and pore distribution per foam. Unlike Foams A and B, Foam C showed a tenfold increase with a porosity increase of only 1.3%. To explain the various strengths of the porosity vs. MFIS relationship, a simple model is proposed here. For this purpose, the foam is described in terms of percolating networks of "hard links" and "soft links". The porous frame work can be thought of as a system of bridging struts connecting at nodes (Fig. 4a). We consider a binary classification of struts distinguishing hard and soft links by taking the local twinning stress as figure of merit for each strut. The local twinning stress of hard links exceeds the magnetostress [2] and, hence, twin boundary motion cannot be induced by a magnetic field. In contrast, in soft links, twin boundaries can move at a low stress level allowing for a significant local MFIS.

Twin boundary motion can promote straining (typical for MFIS) and bending (observed in MSMA wires [25]). Bending is the elementary deformation mode supporting plastic hinging at nodes [26,27]. If a hard link is isolated, i.e. surrounded by soft links, then the strain gradient between hard and soft links can easily be accommodated by hinging and straining of the soft links surrounding the hard link. Thus, an isolated hard link is ineffective regarding stiffening the overall foam. If, on the other hand, hard links form a percolating network (Fig. 4a, dashed line), then local straining and hinging cannot produce a global strain.

Grain boundaries effectively suppress magnetic-field-induced twin boundary motion. For the purpose of this discussion, we assume that grain boundaries are the only hardening agents. For simplicity, we assume that grain boundaries pass through nodes. This assumption is justified by the grain structure. Neutron diffraction studies revealed grain sizes in the millimeter size range [28]. The grains are larger than large pores. Grain boundaries pass through nodes or through entire struts. Only few struts have grain boundaries and if they do, the grain boundary may be considered as a node between two struts. Thus, effectively, there are monocrystalline struts and nodes that may contain a grain boundary. Optical microscopy show struts to be comprised of one main twin variant supporting the assumption that the struts do not contain a grain boundary [16].

Fig. 4 shows a schematic of a foam constructed by a network of struts and nodes with a monomodal pore size distribution (Fig. 4a), as well as a view of the struts and nodes identified in a micrograph (Fig. 4c). Hence, we may consider nodes to constrain local MFIS. The nodes or grain boundaries constrain a volume near the node, (illustrated in Fig. 4b, [29,30]). Assuming a constant cross section, the unconstrained alloy volume fraction (v_{free}) is:

$$v_{free} = 1 - \frac{w}{l}\tan(\alpha) \tag{1}$$

where w is the strut width, l is the strut length, and α is the angle between the twin boundary normal and the strut axis. In a simple binary classification, we may define a strut to be a soft link if its unconstrained volume is finite. Hence, thick and short struts are hard because they have little or no free volume, while thin and long struts are soft because they have a large amount of free volume. The critical value of the strut aspect ratio $(l/w)_c$ between a soft and hard link then depends on the angle α through Eq. (2) with $v_{free} = 0$:

$$\left(\frac{l}{w}\right)_c = \tan(\alpha) \tag{2}$$

Therefore, the critical aspect ratio will predict whether a strut is hard or soft and will depend on α. The inclination angle α depends on the crystallographic orientation of the

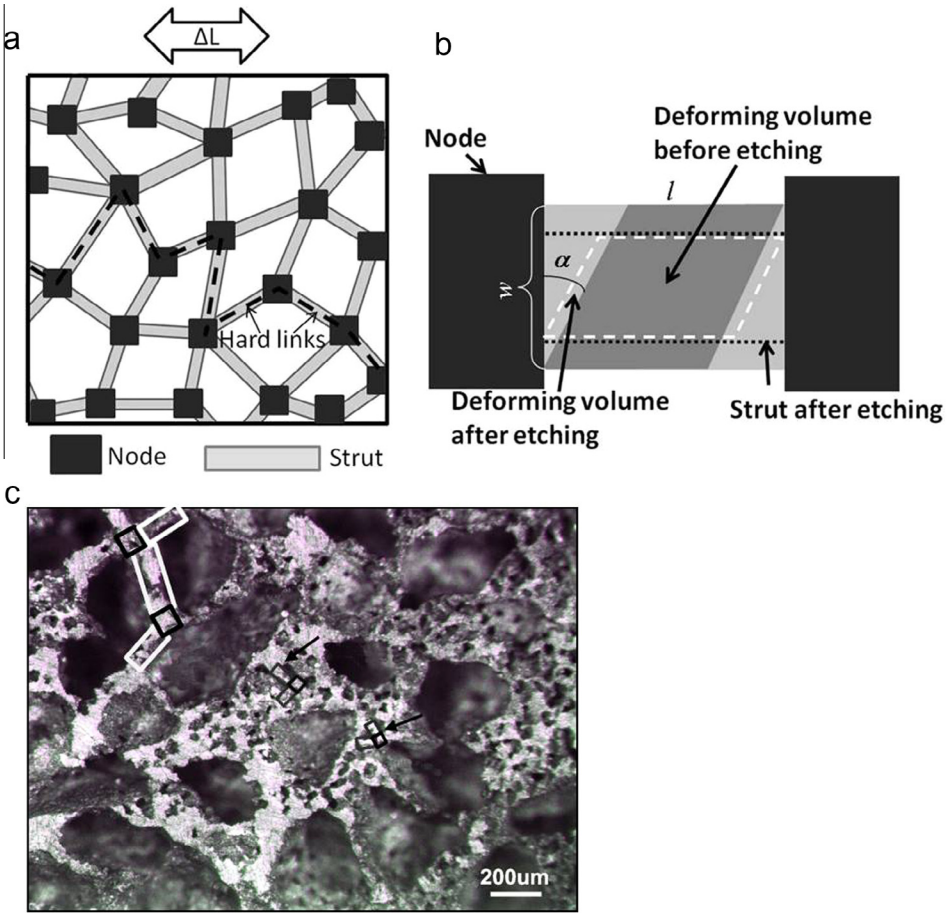

Fig. 4. Schematic showing (a) a network of struts and nodes with hard links (black dashed line) connected together in a hard chain. In the direction indicated by the arrow, the hard chain hinders deformation. (b) A single strut (gray) between two hard nodes (black). The light gray area marks the constrained volume. The dark gray area marks the freely deforming volume before dissolution. When the strut is etched, its width decreases to the dotted line and the fraction of its volume that can deform (dashed white line) increases. (c) Micrograph of a foam with a bi-modal pore distribution; large struts containing small pores are outlined with white rectangular boxes, small struts between small pores are outlined with rectangular black boxes (arrows), and nodes are outlined in black squares similar to the schematic in (a).

strut crystal with respect to the physical orientation of the strut (i.e. architecture). Crystallographic texture and the architecture of foam will impact the variance of α within the foam. A randomly textured foam has a large variance of α implying a large distribution of v_{free} and critical strut aspect ratio $(l/w)_c$; thus, hard and soft links are distributed in the network.

This analysis shows that with increasing porosity the strut aspect ratio increases. This leads to an increased fraction of soft links. Eventually, the soft links break up a percolating network of hard links which leads to a substantial increase of MFIS.

4.2. Effect of pore size and strut aspect ratio

We devise a simple structural model of foam (Fig. 5a). For the foam with one population of pore sizes, we assume struts with length l, width w, and a square cross section arranged along the edges of a cubic lattice. Thus, nodes are cubes with edge w and pores have a width $w + l$. The relationship between porosity p and inverse aspect ratio w/l is shown with a solid line in Fig. 5b. The numbers 1:0 indicate that all pores belong to the large population. The vertical dashed lines indicate $(w/l)_c$, i.e. the separation of soft and hard links for a particular angle α (defined in Fig. 4b). Soft links are located to the left of the dashed line.

The dashed and dotted curves indicated with 0.27:0.73 and 0.5:0.5 show the p vs. w/l relationships for foams with two populations of pore sizes, one small and the other large, mimicking the cast foams with bimodal pore-size distribution. The fractions of small and large pores have a ratio of 50:50 for the dotted line and 27:73 for the dashed line.

The range of critical porosities which separates soft links from hard links extends from 65% to 85% for the foam with 50% large pores and from 81% to 91% for the foam with 73% large pores. Thus, the range of porosity, for which hard and soft links coexist, becomes narrower with increasing relative amount of large pores. At the same time, the range of coexisting hard and soft links is shifted to larger porosity. This is due to the role of large pores, which act to remove all struts, i.e. soft links and hard links alike.

Foam dissolution, by increasing the strut aspect ratio, reduces the fraction of constrained (or hard) volume (light gray area in Fig. 4b) and increases the volume of unconstrained (or soft) material (dotted white line Fig. 4b) within each strut. In particular, dissolution can easily reduce the inverse strut aspect ratio to below the critical value thus

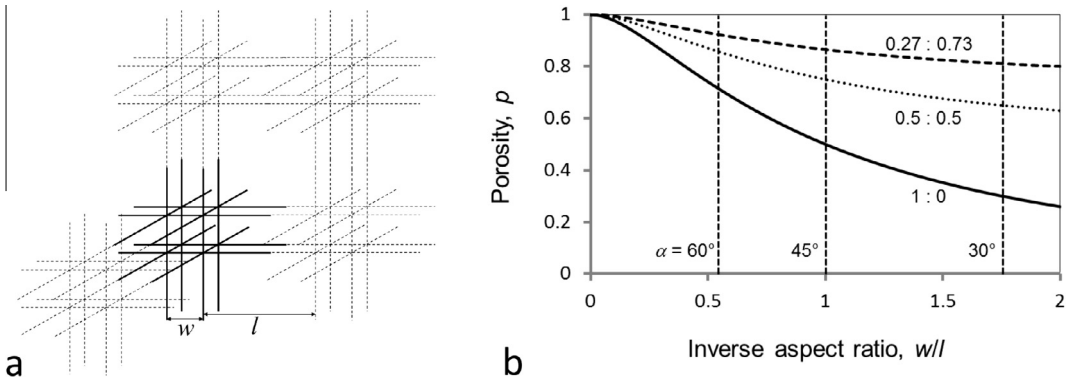

Fig. 5. (a) Schematic of a foam with struts of length l and diameter w. (b) Plot of foam porosity vs. inverse of strut aspect ratio for model shown in (a) with monomodal pore size (solid line), and bimodal pore size distribution: with 50% small pores (dotted line) and with 27% small pores (dashed line). The vertical dashed lines indicate the critical transition from soft links to hard links (with increasing w/l) for the twin boundary inclination angles α of 30°, 45°, and 60°.

transforming hard links into soft links. Translated to Fig. 5b, this means moving from the bottom right (region of hard links) to the top left (region of soft links) along the line appropriate for a particular ratio of small and large pores. For a foam with small pores, a small change of porosity reduces w/l more than for a foam with monomodal pore size distribution. Thus, a small change in porosity increases the fraction of soft links much more effectively for foams with many small pores in large primary struts.

So far, we considered only grain boundaries as sources for hard links. A second possibility is represented by remaining space-holder material, which prevents deformation of the foam in its vicinity. As residual space holders are expected to be removed by the acid during the metal dissolution step, this represents a second mechanism of transforming hard links into soft links via dissolution.

A third mechanism by which a non-linear effect may occur is given if a significant amount of hard links is broken or etched enough such that connectivity of the percolating network of hard links is no longer maintained, the deformation of the whole network of struts can occur to a much higher degree. In this manner too, a small overall porosity increase may be sufficient to remove continuous hard links in the bimodal foam.

This hard link hypothesis may explain why Foam C had such a strong increase in MFIS after a very modest porosity increase. In Fig. 1a, Foam C initially showed no martensitic phase transformation hysteresis but a slow decline in MFIS which might be expected due to the dependency of magnetic anisotropy on temperature [31,32]. Severe cracking, as observed after TMC (Fig. 1d), is indirect evidence that space-holders were present during the initial testing due to incomplete removal in acid. The crack ledges are displaced implying that the material deformed after being initially cracked, suggesting the space holders were only present during the first TMC. During TMC, the hard ceramic restricted the deformation in the Ni–Mn–Ga metal, which was accommodated by cracking within the metal. If the residual space holders were present during the first TMC testing, enough constraint could be imposed to form a percolating network of hard links such that the foam did not deform and therefore no martensitic phase transformation was observed. During the first dissolution step, the space-holder may have been removed completely, allowing the material to deform. The cracks together with the dissolution (which removes remaining ceramic and thins struts), thus broke the hard link network and lead to the dramatic increase in MFIS. It seems that breaking the hard links is much more effective at releasing internal constraint in the networks of struts than metal dissolution.

4.3. Texture and pore size distribution

The different rates of MFIS increase with porosity increase among Foams A, B, and C may be due to crystallographic texture and/or pore distribution differences among foams. The magneto crystalline anisotropy energy for the foams was 5% (foam B) and 20% (A and C) of that expected for a single crystal. A randomly oriented polycrystal would be expected to show 0% of the single crystal anisotropy energy. Thus, the foams were polycrystalline with a slightly preferred orientation. The varying magneto-crystalline anisotropy energy among the three foams indicates different levels of crystallographic texture. Texture enhanced MFIS in polycrystalline, pore-free materials is expected due to reduced constraints at grain boundaries [11–14]. The same enhancement can be expected in the foam. Further, the free volume [v_{free}, Eq. (1)] depends on the twin boundary orientation within the struts (inclination angle α). The twin orientation within the strut dictates the rate of free volume increase with strut thinning. Even though some texture is present in the foam, texture is not expected to change with dissolution, and therefore enhancement of MFIS in Ni–Mn–Ga foam cannot be attributed to texture variation. Texture will however impact the strength of the effect of porosity on MFIS and the trainability through the inclination angle α (Eq. (2)), which controls the ability of a given strut to deform (i.e. to be weak or hard).

The distribution of small and large pores may also have a large impact on how effective etching relieves constraints and may be another reason for different slopes shown in Fig. 2. For segregated large pores, the local state resembles that of a foam with monomodal pore size distribution. Hence, transition from percolating to non-percolating network occurs in such regions over a wider porosity range (full line in Fig. 5). Thus, with segregated small and large pores, the probability of a percolating network of hard links is larger than for homogeneously distributed small and large pores. Therefore, the pore distribution may dictate the distribution of hard links and possibly the connectivity of the percolating network.

Foam C also showed a clear training effect resulting from TMC, demonstrated by an increase in maximum MFIS with each TMC. During TMC, not only is a particular twinning system preferred during the martensite formation by the application of a magnetic field, but additionally the rotating field favors twinning systems that are also mobile in the plane of the rotating field. In Fig. 1b, the first TMC follows the same MFIS vs. temperature path, while in the martensite phase, for both heating and cooling curves. However, for the subsequent TMCs, this does not hold true. In the first TMC, the foam is most likely self-accommodated which would explain the slowly decreasing MFIS up to the phase transformation. Incompatible twinning systems interfere with each other as rotation of the magnetic field proceeds [2,5,33,34]. After the first TMC, the foam is now in a trained state, showing constant MFIS up to the M–A phase transformation. Once trained, it is possible that, during cooling with a rotating field, certain twinning systems become inactive and remain so even upon heating [2,5,33,34]; deactivated twinning systems cause the MFIS in the martensite phase to be lower upon heating than upon previous cooling.

Fig. 2 shows the second TMCs of Foam B for porosity values 54.8% and 56.6% and the third TMC of Foam B for 60.3% porosity. These TMCs were chosen because they showed the largest MFIS for each porosity step. The maximum level of MFIS from lower porosity to higher porosity increased as well as the martensitic phase transformation hysteresis changes. Both the change in the MFIS and the change in the martensitic phase transformation hysteresis can be explained by removal of the hard links. At the lower porosities, 54.8% and 56.6%, the transformation hysteresis is wide and cooling only gradually increases MFIS. In fact, the highest strain of the thermal cycle occurs during heating at the lower porosities. This is in contrast to Foam B at 60.3% porosity. There is a sharp increase in MFIS upon cooling and the transformation hysteresis is narrower. The hard links may act as three-dimensional constraints for the whole foam network and require more undercooling for the martensitic phase transformation to complete [35–37]. Overall, in the light of the hard link concept, the variations between the thermo-magneto-mechanical training and hysteresis of various foams probably reflect the effects of various distributions of hard links due to combinations of grain orientations, sizes and grain boundary location.

Each foam experienced failure after the final dissolution step. Ni alloys are easily passivated by a chemisorbed layer of either sulfur or oxygen; since Ni–Mn–Ga is 50% Ni, the same may be true for the alloy as well [38–40]. Local breakdown of the passive layer in the deformation area may be appreciable during magnetic-field-induced deformation. The regions of breakdown in the chemisorbed layer may be etched at a much higher rate than the surrounding area. Therefore, the combination of dissolution and deformation experiments may have contributed to a small number of dissolution steps that could be performed before failure occurred. Further experimental observations are needed, e.g. by tomography, to test this hypothesis.

5. Conclusions

Experiments using acid dissolution to increase porosity in polycrystalline Ni–Mn–Ga foams, while maintaining a constant composition, grain size, and texture, show that porosity increase is responsible for the enhanced MSME observed in these foams, supporting the original hypothesis [15,17] based on reduction of internal constraints. Heating and cooling the foam in a rotating magnetic field provides effective training to increase MFIS. A method of relating twin orientation and strut dimensions was developed to classify struts as soft links (able to deform induced by a magnetic field) or hard links (unable to deform induced by a magnetic field). The results were discussed in terms of the concept of a percolating hard link network. Transforming hard links into soft links by strut cracking or thinning may result in a dramatic increase in MFIS. The cracking that occurred during initial testing removed hard links. Once the residual space holders were removed, the connectivity of the percolating hard link network was broken, resulting in a much higher global MFIS. Strut thinning or increasing porosity reduced the cross section of struts with constant length, hence increased the strut aspect ratio. Increasing the strut aspect ratio increased the deforming (free) volume in the struts and softened the link. Similar to cracking, if even one hard link is softened with thinning, the connectivity of the hard percolating network can be broken. The amount and distribution of hard links may be determined by the pore distribution and crystallographic orientation within the strut which can be highly variable from specimen to specimen and may contribute to the different strength of the dependence of MFIS on porosity. Foam C at the highest porosity showed a notable training effect. The present results imply that properties such as MFIS and transformation hysteresis can be tailored with the level of porosity.

Acknowledgments

The authors acknowledge financial support from the National Science Foundation, Division of Materials Research through grant No. DMR-1207192 (BSU) and Grant No. DMR-1207282 (NU). MC acknowledges financial support of the German Research Foundation (DFG) through the priority program SPP 1239 (Grant No. Schn 1106). PM is thankful to ETH Zürich, Switzerland, for donating magneto-mechanical testing devices.

References

[1] R.D. James, M. Wuttig, Philos. Mag. A 77 (1998) 1273.
[2] P. Müllner, V.A. Chernenko, M. Wollgarten, G. Kostorz, J. Appl. Phys. 92 (2002) 6708.
[3] S.J. Murray, M. Marioni, S.M. Allen, R.C. O'Handley, T.A. Lograsso, Appl. Phys. Lett. 77 (2000) 886.
[4] K. Ullakko, J.K. Huang, C. Kantner, R.C. Ohandley, V.V. Kokorin, Appl. Phys. Lett. 69 (1996) 1966.
[5] P. Müllner, V.A. Chernenko, G. Kostorz, J. Appl. Phys. 95 (2004) 1531.
[6] A. Sozinov, A.A. Likhachev, N. Lanska, K. Ullakko, Appl. Phys. Lett. 80 (2002) 1746.
[7] P. Lazpita, G. Rojo, J. Gutierrez, J.M. Barandiaran, R.C. O'Handley, Sens. Lett. 5 (2007) 65.
[8] M. Pasquale, C. Sasso, S. Besseghini, E. Passaretti, E. Villa, A. Sciacca, IEEE Trans. Magn. 36 (2000) 3263.
[9] R. Chulist, W. Skrotzki, C.G. Oertel, A. Böhm, M. Pötschke, Scripta Materialia 63, 548.
[10] U. Gaitzsch, M. Pötschke, S. Roth, B. Rellinghaus, L. Schultz, Scr. Mater. 57 (2007) 493.
[11] U. Gaitzsch, M. Pötschke, S. Roth, B. Rellinghaus, L. Schultz, Acta Mater. 57 (2009) 365.

[12] M. Pasquale, C.P. Sasso, S. Besseghini, F. Passaretti, E. Villa, V.A. Chernenko, J. Phys. IV 11 (2001) 305.
[13] M. Pötschke, U. Gaitzsch, S. Roth, B. Rellinghaus, L. Schultz, J. Magn. Magn. Mater. 316 (2007) 383.
[14] M. Pötschke, S. Weiss, U. Gaitzsch, D.Y. Cong, C. Hürrich, S. Roth, L. Schultz, Scripta Mater. 63, 383.
[15] Y. Boonyongmaneerat, M. Chmielus, D.C. Dunand, P. Müllner, Phys. Rev. Lett. 99 (2007) 247201.
[16] M. Chmielus, X.X. Zhang, C. Witherspoon, D.C. Dunand, P. Müllner, Nat. Mater. 8 (2009) 863.
[17] X.X. Zhang, C. Witherspoon, P. Müllner, D.C. Dunand, Acta Mater. 59 (2011) 2229.
[18] M. Frary, C.A. Schuh, Appl. Phys. Lett. 83 (2003) 3755.
[19] M. Frary, C.A. Schuh, Phys. Rev. B 69 (2004) 13.
[20] M. Frary, C.A. Schuh, Acta Mater. 53 (2005) 4323.
[21] M. Frary, C.A. Schuh, Philos. Mag. 85 (2005) 1123.
[22] Y. Boonyongmaneerat, D.C. Dunand, Adv. Eng. Mater. 10 (2008) 379.
[23] Y. Matsumoto, A.H. Brothers, S.R. Stock, D.C. Dunand, Mat. Sci. Eng. A 447 (2007) 150.
[24] A. Sozinov, A.A. Likhachev, K. Ullakko, IEEE Trans. Magn. (2002) 38.
[25] P. Zheng, N.J. Kucza, C.L. Patrick, P. Müllner, D.C. Dunand, J. Alloys Comp. 624 (2015) 226.
[26] L.J. Gibson, M.F. Ashby (Eds.), Cellular Solids: Structure and Properties, Cambridge University Press, Cambridge, U.K., 1997.
[27] M.F. Ashby, A.G. Evans, N.A. Fleck, L.J. Gibson, J.W. Hutchinson, H.N.C. Wadley (Eds.), Metal Foams: A Design Guide, Butterworth Heinemann, Oxford, 2000.
[28] C. Witherspoon, P. Zheng, M. Chmielus, S.C. Vogel, D.C. Dunand, P. Müllner, Acta Mater. 61 (2013) 2113.
[29] M. Chmielus, I. Glavatskyy, J.-U. Hoffmann, V.A. Chernenko, R. Schneider, P. Müllner, Scr. Mater. 64 (2011) 888.
[30] C.P. Henry, D. Bono, J. Feuchtwanger, S.M. Allen, R.C. O'Handley, J. App. Phys 91 (2002) 7810.
[31] O. Heczko, L. Straka, J. Appl. Phys. 94 (2003) 7139.
[32] O. Heczko, L. Straka, N. Lanska, K. Ullakko, J. Enkovaara, J. Appl. Phys. 91 (2002) 8228.
[33] I. Aalito, A. Soroka, Y. Ge, O. Söderberg, S.P. Hannula, Smart Mater. Struct. 19 (2010) 075014.
[34] M. Chmielus, V.A. Chernenko, W.B. Knowlton, G. Kostorz, P. Müllner, Eur. Phys. J. Spec. Top. 158 (2008) 79.
[35] I. Karaman, H.E. Karaca, B. Basaran, D.C. Lagoudas, Y.I. Chumlyakov, H.J. Maier, Scr. Mater. 55 (2006) 403.
[36] M. Richard, J. Feuchtwanger, D. Schlagel, T. Lograsso, S.M. Allen, R.C. O'Handley, Scr. Mater. 54 (2006) 1797.
[37] M.L. Richard, J. Feuchtwanger, S.M. Allen, R.C. O'Handley, P. Lazpita, Metall. Mater. Trans. A 38A (2007) 777.
[38] A. Gebert, S. Roth, S. Oswald, L. Schultz, Corros. Sci. 51 (2009) 9.
[39] P. Marcus, E. Protopapoff, J. Electrochem. Soc. 140 (1993) 5.
[40] J. Osterwald, H.H. Uhlig, J. Electrochem. Soc. 108 (1961) 5.